Modelling of SF_6 Arc in a Supersonic Nozzle.　Part I: Cold Flow Features and DC Arc Characteristics

Q Zhang, J D Yan and M T C Fang

Department of Electrical Engineering and Electronics, University of Liverpool, Brownlow Hill, Liverpool L69 3GJ, UK

Email: quan323@liv.ac.uk, yaneee@liv.ac.uk and ee24@liv.ac.uk

Abstract. The cold flow and the arc under direct currents burning in the nozzle of [1] with fixed stagnation pressure have been investigated computationally using five flow models, which include laminar flow model, the Prandtl mixing length model, the standard k-epsilon model and its two variants, Chen-Kim model and RNG model. For the cold flow, computational results are nearly the same for different flow models except in the region close to two electrodes. There is a bow shock in front of the downstream hollow electrode and a wake near the tip of the upstream electrode. The size of the wake and the strength and the structure of the shock differ widely with the flow models. With a DC arc in the nozzle, derived voltage-current characteristics are negative for currents less than 600 A but for higher currents arc voltage is nearly constant.

1 Introduction

Almost all high voltage circuit breakers now use SF_6 and when in operation produce arcs in supersonic flow. For such an arcing environment it is well known that turbulence plays a critical role in the determination of the critical rate of rise of recovery voltage (RRRV) which a breaker can withstand after current zero [2]. In spite of the relatively long history since the confirmation of arc turbulence [3], modelling of turbulent arc is still at its infancy as the mechanisms for generating arc instability and maintaining turbulence in the arc context are little understood. Therefore, no turbulence models have so far been specifically devised for arc plasmas. An arc in a supersonic nozzle is similar to a shear boundary layer in that the axially dominant flow inside the arc attains a much higher speed than that of its surrounding cold flow. Moreover, the axial momentum and energy diffusion can be neglected in comparison with their radial counterparts when the radial extent of the arc is much less than the arc length [4]. Thus, there is a direct resemblance between a high velocity round free jet in a stagnant external flow and an arc surrounded by a cold and low speed flow in a nozzle. This is the reason why turbulence models designed for incompressible and constant property shear boundary layers have been used to account for the turbulent effects of an SF_6 arc burning in a supersonic nozzle [2, 5, 6].

Up to now, the commonly used models for turbulent nozzle arcs suitable for engineering applications are based on the concept of eddy viscosity which requires the knowledge of a velocity and a length scale characterizing the turbulence [7]. Turbulence models provide the means for the determination of these two characteristic quantities with closure assumptions which inevitably introduce arbitrary constants [7]. These constants are adjusted according to experimental results to give optimal prediction for a specific type of turbulent flow. Of the turbulence models based on eddy viscosity the Prandtl mixing length model has achieved considerable success in predicting turbulent arc behavior [2]. The standard k-epsilon model with the default values of the five turbulence parameters [8] and two of its variants (the renormalization group, commonly known as the RNG model [9] and Chen-Kim model [10]) have been used for the modelling of the turbulent flow in circuit breakers with contradictory claims regarding their successes [5, 6, 11, 12, 13]. The test conditions in terms of current, pressure and system geometry covered by the aforementioned investigations are however very limited. Hence, no general conclusions on the relative merits of the turbulence models so far employed can be drawn. The verification of turbulence models suitable for switching applications requires extensive reproducible experimental results covering a wide range of test conditions. Such experimental data is extremely scarce.

Extensive test results given in the form of RRRV have been reported for a supersonic nozzle interrupter with fixed upstream and downstream pressures by Benenson et.al [1]. The arc behaviour and its thermal interruption capability are investigated by using a current ramp consisting of a plateau (DC level) and a linearly decaying current (specified by di/dt) before current zero and a voltage ramp (specified by dV/dt) after current zero [1]. Such a two-pressure system eliminates pressure transients caused by wave reflections within a circuit breaker which inevitably affects the arc in the nozzle interrupter. Thus, the test results of RRRV given [1] are well suited for the verification of turbulence models from which appropriate conclusions can be drawn as regards the relative merits of turbulence models employed in the present investigation (details to be given in Section 2).

Preliminary investigation [14] of SF_6 nozzle arc indicates that the differences in arc voltages predicted by the aforementioned four turbulence models at the plateau of a current ramp, 1 kA DC, are less than 15% of each other, which is well within the experimental scatter normally encountered during the tests of circuit breakers. This result seems to indicate that turbulence at high currents is not a decisive factor for the determination of arc voltage. This appears to be in agreement with a DC nitrogen nozzle arc at 2 kA for which laminar theory can give a satisfactory account of the arc behaviour [15]. This prompts the current investigation into the role of turbulence in DC SF_6 nozzle arcs.

The present investigation (Part I) forms a part of a systematic investigation into the behaviour of SF_6 nozzle arc. Part I (the present paper) is concerned with the studies of the flow features in the absence of the arc (hereafter referred to as the cold flow) as well as with a detailed study of the arc behavior under different DC currents. Part II (a sequential paper) is exclusively concerned with the arc behavior under a current ramp before current zero and a voltage ramp after current zero. The computed RRRV will be compared with those reported in [1]. Relative merits of turbulence models employed will be discussed in detail in Part II. The influence of nozzle geometry on the arc characteristics and on RRRV will be studied in Part III.

No experimentally measured DC arc voltages for the nozzle used in [1] are available for direct comparison with the computational results reported in Part I. However, the importance of cold flow on the dielectric strength and the effects of different choices of DC currents for the plateau of the current ramp on RRRV warrant a detailed report of computational results at two different stagnation pressures [1].

The paper is organized as follows. Section 2 gives the reasons for the choice of the four turbulence models used in the present investigation and their corresponding governing equations. Details of the computation domain and the boundary conditions prescribed are presented in Section 3. Cold flow features and the effects of upstream and downstream electrodes on the flow are discussed in Section 4. This is followed by a discussion of DC arc-flow interaction, the arc features and the DC arc voltage-current characteristics as predicted by the four turbulence models and the laminar flow model. Finally, appropriate conclusions are drawn.

2 The governing equations and turbulence models

2.1 The governing equations

The arc together with its surrounding cold gas flow is assumed under local thermodynamic equilibrium (LTE), which can be described by the following conservation equation in cylindrical coordinates assuming axisymmetry:

$$\frac{\partial(\rho\phi)}{\partial t} + \frac{1}{r}\frac{\partial}{\partial r}\left[r\rho v\phi - r\Gamma_\phi\frac{\partial\phi}{\partial r}\right] + \frac{\partial}{\partial z}\left[\rho w\phi - \Gamma_\phi\frac{\partial\phi}{\partial z}\right] = S_\phi \tag{1}$$

For turbulent flow equation (1) is the time averaged conservation equation [7], where ϕ is the dependent variable and ρ the gas density. v and w are, respectively, the radial and axial velocity components. The source terms and the diffusion coefficients are listed in Table 1 for different conservation equations, in which all notations have their conventional meaning. The subscript l denotes the laminar part of the transport coefficient and t the turbulent part. Laminar (molecular) viscous stresses and turbulent (Reynolds) stresses are taken into account by the diffusion terms on the left-hand side of the two momentum equations in Table 1. The part of the viscous and turbulent stresses in the radial momentum equation which cannot be written as part of the diffusion term is included in the source term. It has been found that molecular viscous effects are negligible in momentum balance for arcs in a supersonic nozzle even under laminar flow conditions [15]. Ohmic heating and radiation are given in the source term of the enthalpy equation, which also includes the viscous heating due to molecular and turbulent stresses. The Lorentz force generated by the interaction of the arc current with its own magnetic field can be neglected for currents below 2 kA in a supersonic nozzle [15].

Table 1. Terms of governing equations.

Equation	ϕ	Γ_ϕ	S_ϕ
Continuity	1	0	0
Z-momentum	w	$\mu_l + \mu_t$	$-\dfrac{\partial p}{\partial z}$
R-momentum	v	$\mu_l + \mu_t$	$-\dfrac{\partial p}{\partial r} - \left(\mu_l + \mu_t\right)\dfrac{v}{r^2}$
Enthalpy	h	$\dfrac{k_l + k_t}{c_p}$	$\dfrac{dp}{dt} + \sigma E^2 - q + \left(\mu_l + \mu_t\right)\left\{2\left[\left(\dfrac{\partial v}{\partial r}\right)^2 + \dfrac{v^2}{r^2} + \left(\dfrac{\partial w}{\partial z}\right)^2\right] + \left(\dfrac{\partial v}{\partial z} + \dfrac{\partial w}{\partial r}\right)^2\right\}$

The equation of state and the transport coefficients of SF_6 including electrical conductivity are determined by temperature and pressure, which have been tabulated by Frost and Liebermann [16]. For the present investigation, the arcing current does not exceed 1 kA. The axial electrical field, E, can therefore be considered to be constant over the arc cross-section, which can be calculated by the simplified Ohmic law

$$i = E\int_0^\infty \sigma 2\pi r dr \tag{2}$$

where i is the instantaneous current and σ is the electrical conductivity. For an axisymmetric arc with monotonically decreasing radial temperature, net radiation loss, q, in enthalpy equation is calculated with the approximate model of Zhang et al [15]. Relevant details of the radiation model are well presented in [15], which needs not be repeated here.

By setting μ_t and k_t to zero we obtain the laminar flow model. Computational results of the laminar flow model will be used to judge the importance of turbulence on the arc behaviour.

2.2 Turbulence models

There are a large number of turbulence models [7, 8, 9, 10, 17]. However, there is no general theoretical guidance regarding the choice of turbulence models for turbulent arcs in supersonic flow. Our choice of turbulence models is restricted to those which have been applied with success to similar flow conditions as those of an arc burning in a supersonic flow as well as their suitability for engineering application (low computational cost). Thus, we choose those turbulence models which belong to the category of effective eddy viscosity. Reynolds stresses are linearly linked to the main strain via eddy viscosity by means of Boussinesq hypothesis [7]. Four turbulence models given below have been chosen for our investigation as they have achieved considerable success in the prediction of the behavior of turbulent thin shear layers.

As the eddies in a turbulent flow moves randomly in a manner similar to molecular random motion, in direct analogy to the diffusion coefficient of a gas, eddy viscosity is assumed to be related to a length and a velocity scale charactering the random motion of the large scale eddies which interact actively with the mean flow:

$$\mu_t = C_\mu \rho \lambda_c V_c \tag{3}$$

where C_μ is a constant and λ_c and V_c are respectively the length and velocity scale of the turbulent motion. Turbulence models provide sufficient number of equations to calculate these two characteristic quantities. Turbulent Prandtl number provides the link between eddy viscosity (μ_t) and turbulent thermal conductivity (k_t) in equation (1).

2.2.1 The Prandtl mixing length model

This is the simplest and also the oldest turbulence model which relates the turbulence length scale to the width of the jet. For turbulent nozzle arc this length scale marks the boundary of the high velocity core which is measured by the thermal radius of the arc defined by [18]

$$r_\delta = \left(\theta_\delta/\pi\right)^{1/2} \tag{4}$$

where θ_δ is the thermal area of the arc given by

$$\theta_\delta = \int_0^\infty \left(1 - \frac{T_\infty}{T}\right) 2\pi r dr \tag{5}$$

where T_∞ is the temperature near the nozzle wall where the radial temperature gradient is negligible. Turbulence length scale is related to the thermal radius by

$$\lambda_c = c r_\delta \tag{6}$$

where c is a turbulence parameter the value of which is found by the best fit between model prediction and experimental results. The velocity scale is related to the turbulence length scale and the mean velocity gradient by

$$V_c = \lambda_c \left(\left|\frac{\partial w}{\partial r}\right| + \left|\frac{\partial v}{\partial z}\right|\right) \tag{7}$$

Eddy viscosity is given by

$$\mu_t = \rho \lambda_c^2 \left(\left|\frac{\partial w}{\partial r}\right| + \left|\frac{\partial v}{\partial z}\right|\right) \tag{8}$$

2.2.2 The standard k-epsilon model

This model with the recommended default values for the five turbulence parameters [8] is the most widely used turbulence model for engineering applications. This model has been applied to DC nozzle arcs [5] and to DC plasma jets [11, 12].

The equations of the standard k-epsilon model are those for the turbulent kinetic energy per unit mass, k, and the dissipation rate, ε, which are given below:

$$\frac{\partial(\rho k)}{\partial t} + \nabla \cdot \left(\rho \vec{V} k - \frac{\rho \nu_t}{\sigma_k} \nabla k\right) = \rho(P_k - \varepsilon) \tag{9}$$

$$\frac{\partial(\rho \varepsilon)}{\partial t} + \nabla \cdot \left(\rho \vec{V} \varepsilon - \frac{\rho \nu_t}{\sigma_\varepsilon} \nabla \varepsilon\right) = \rho \frac{\varepsilon}{k}\left(C_{1e} P_k - C_{2e} \varepsilon\right) \tag{10}$$

where P_k represents the generation of turbulence kinetic energy due to the mean velocity gradients, which is given by

$$P_k = v_t \left[2\left(\frac{\partial w}{\partial z}\right)^2 + 2\left(\frac{\partial v}{\partial r}\right)^2 + 2\left(\frac{v}{r}\right)^2 + \left(\frac{\partial w}{\partial r} + \frac{\partial v}{\partial z}\right)^2 \right] \tag{11}$$

The length and velocity scales of turbulence are respectively defined as

$$\lambda_c \propto \frac{k^{1.5}}{\varepsilon} \tag{12}$$

$$V_c \propto \sqrt{k} \tag{13}$$

Eddy viscosity is thus given by the following expression according to equation (3):

$$\mu_t = \rho C_\mu \frac{k^2}{\varepsilon} \tag{14}$$

There are altogether five model constants in the k-epsilon model equations, the value of which have been adjusted according to test results for a range of fluid flows. The recommended values of these constants are [8]: $\sigma_k = 1.0$, $\sigma_\varepsilon = 1.3$, $C_{1e} = 1.44$, $C_{2e} = 1.92$ and $C_\mu = 0.09$.

2.2.3 The Chen-Kim k-epsilon model

It has been recognized that the poor prediction of the spread rate of a turbulent round free jet by the standard k-epsilon model is due to the inadequacy of the equation for dissipation rate [10]. For the standard k-epsilon model a single time scale, k/ε, is used which is an over simplification of various time scales associated with energy transfer between eddies of different sizes [10]. A second time scale related to production of turbulent kinetic energy is thus introduced to reflect the energy transfer rate from large scale eddies to small scales eddies controlled by the production range time scale to the dissipation range time scale, P_k/ε [10]. The additional source term

$$S_\varepsilon = \frac{\rho C_{3e} P_k^2}{k} \tag{15}$$

is added to equation (10), which allows the dissipation rate equation to respond to the mean strain rate more efficiently especially in the region where the main strain rate changes rapidly. Such a situation exists inside a supersonic nozzle. Because of the success of the Chen-Kim k-epsilon model in the prediction of the spread rate of a turbulent round jet which is similar to an arc burning in a supersonic flow, we apply this model to the DC nozzle arc.

The constant, $C_{3e,}$ and the other constants in the standard k-epsilon model are readjusted to achieve best agreement between prediction and experimental results covering a wide range of flow conditions [10]. The recommended values for these constants are [10]: $\sigma_k = 0.75$, $\sigma_\varepsilon = 1.15$, $C_{1e} = 1.15$,

$C_{2e} = 1.90$ $C_{3e} = 0.25$, and $C_\mu = 0.09$.

2.2.4 The RNG k-epsilon model

The RNG k-epsilon model is derived from the instantaneous Navier-Stokes equation using a mathematical approach called the renormalization group [9]. The effects of the small scale turbulence are represented by means of a random forcing function in the Navier-Stokes equation. The RNG procedure systemically removes the small scale eddies from the governing equations by expressing their effects in terms of large scale eddies through the modified viscosity (i.e. ν_t in Equations (10) and (11) is replaced by the effective viscosity $\nu_{eff} = \nu_l + \nu_t$ where ν_l is the molecular viscosity). In addition, the epsilon equation contains a strain-dependent correction term which is given by

$$S_\varepsilon = -\frac{\rho C_\mu \eta^3 \left(1 - \eta/\eta_0\right)}{1 + \beta \eta^3} \frac{\varepsilon^2}{k} \tag{16}$$

where $\eta = \left(k/\varepsilon\right) \cdot \sqrt{\left(\rho P_k / \mu_t\right)}$, $\eta_0 = 4.38$ and $\beta = 0.012$. The other model constants are [9]:

$\sigma_k = \sigma_\varepsilon = 0.7194$, $C_{1e} = 1.42$, $C_{2e} = 1.68$ and $C_\mu = 0.0845$. In contrast to the standard k-epsilon model only the constant β is adjustable to ensure the best fit with experimental results. The recommended value for β is 0.012. All other constants are explicitly computed as part of RNG process.

The RNG k-epsilon model has been successful in the prediction of plasma jet for arc cutting processes [11] and that for a spray system [12]. It is also claimed successful in predicting the gas mixing in the expansion volume of a circuit breaker [13]. We therefore include this model in our current investigation.

Turbulent thermal conductivity is related to the eddy viscosity through turbulent Prandtl number by

$$\mathrm{Pr}_t = \frac{\mu_t}{\left(k_t / C_P\right)}, \tag{17}$$

where $\mathrm{Pr}_t = 1$ has been assumed.

3 Computational domain and boundary conditions

Computation has been performed on the nozzle used by Benenson et. al [1], the dimensions of which are shown in Figure 1. The distance between two electrodes is 21.5mm. The diameter of the nozzle inlet is 25.4 mm and that of the outlet 38.1 mm. The flat nozzle throat is 4.6 mm long with a diameter of 12.7 mm. The upstream electrode has a round tip and the outer diameter is identical with the nozzle throat diameter. The downstream electrode is hollow. The outer diameter of this electrode is 6.35 mm and the inner diameter is 3.6 mm.
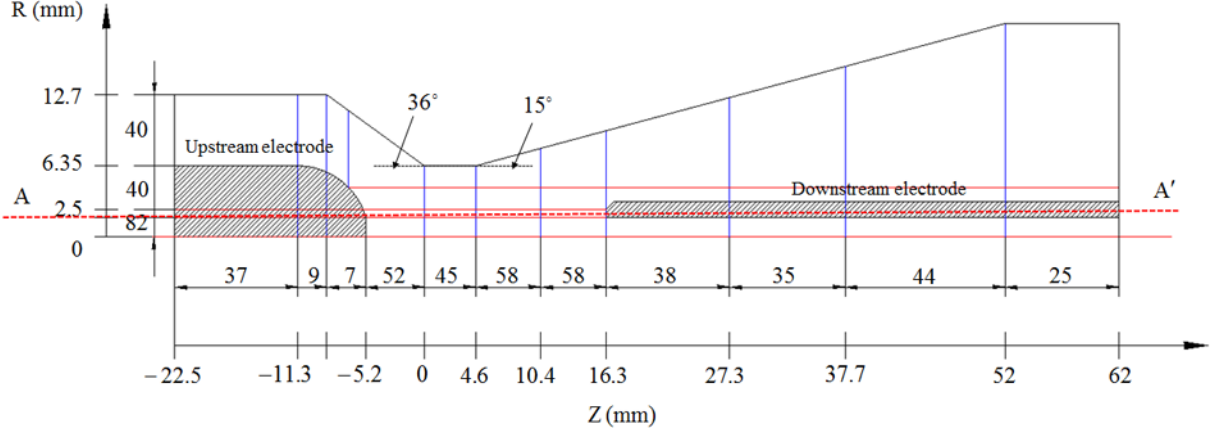
Figure 1. Nozzle geometry and grid system. The computation domain is divided into eleven intervals in the axial direction and four in radial direction. The axial and radial coordinates defining the intervals and the number of cells in each interval are indicated above. Z=0 indicates the axial position of the inlet of flat nozzle throat. There are 162×408 grids. Dense grids are distributed in the arc region with an average grid spacing of 0.1mm in the axial direction.

Version 3.6.1 of PHOENICS has been used to solve the governing equations. The boundary conditions for solutions of the conservation equations are given below:

(a)   On the nozzle axis, axisymmetric boundary conditions are applied. Thus, all radial derivatives of the dependent variables are set to zero except for the radial velocity which is zero on the axis.

(b)   At the nozzle inlet, the axial velocity and density are iteratively computed according to the calculated inlet static pressure by assuming that the gas entering the nozzle undergoes an isentropic process [5, 19] from a reservoir with stagnation pressure P_0 and stagnation temperature T_0 (300 K).

(c)   At the nozzle exit, the static pressure is set to a very low value to guarantee shock free inside the nozzle in the absence of downstream electrode. This is consistent with the test conditions of Benenson et. al [1]. The axial gradients of enthalpy and velocity are set to zero [5].

(d)   At solid surfaces, non-slip boundary condition for velocity is applied through a built-in wall function of PHOENICS [19]. These surfaces are assumed to be adiabatic, for which the heat flux is set to zero.

(e)   When applying the standard k-epsilon model and its two variants, relevant boundary conditions need to be specified. The turbulent kinetic energy and dissipation rate at the nozzle inlet are given by [7, 20]

$$k_{in} = \frac{3}{2}\left(w_{in}I\right)^2 \tag{18}$$

$$\varepsilon_{in} = C_\mu^{3/4}\frac{k_{in}^{3/2}}{\ell} \tag{19}$$

where w_{in} is the nozzle inlet velocity, I the turbulent intensity set at 5% as recommended by [20] and $\ell = 0.07L$. L is the characteristic length of the equipment [7, 20] given by ($d_{inlet} - d_{electrode}$) where d_{inlet} is the diameter of the nozzle inlet and $d_{electrode}$ the electrode diameter. At the nozzle exit, the

axial gradients of k and ε are set to zero.

The arc rooting mechanisms at the upstream and downstream electrodes are not considered. The heat flux into the two electrodes is assumed zero. This ensures that the temperature in front of the upstream electrode is sufficiently high to conduct current. The use of simplified Ohm's law in front of the hollow electrode is equivalent to locating a transparent electrode to collect the current as first suggested by Yan et. al [28]. Arc voltage is dominated by arc column and is not sensitive to the boundary conditions assumed at the upstream electrode [15].

4 Results and discussion

Computations have been carried out for two stagnation pressures (P_0 = 11.2 and 21.4 atm) and for DC currents ranging from 50 A to 1 kA for the nozzle of Figure 1. Results are given for arcs in laminar flow and in turbulent flow as described by the four turbulence models of Section 2. For simplicity arc models based on laminar flow and turbulent flow will be referred to collectively as the flow models for future reference. As there are no DC arc voltage measurements available for the optimization of the turbulence parameter, c, of the Prandtl mixing length model, c is adjusted to give the closest agreement with the measured RRRV in [1] for P_0 = 21.4 atm and di/dt= 25 A/μs. The value of c is 0.048 for the nozzle of Figure 1.

4.1 Features of the cold flow and the influence of upstream and downstream electrodes

4.1.1 General features of the cold flow
Computations of the cold flow have been performed using the flow models previously mentioned. The Prandtl mixing length model is not used for the computation of cold flow as the internal nozzle flow is not of thin shear layer type, thus turbulence length scale being difficult to define. It has been found that the computational results obtained by all flow models are almost identical except in the region close to the upstream electrode tip and to the shock due to the presence of downstream electrode in the supersonic flow region. The qualitative trends of pressure and velocity variations in these two regions are similar although their magnitudes differ greatly depending on the flow models. The results obtained by the standard k-epsilon model are therefore used to illustrate the features of the cold flow.

Figure 2 shows the pressure distribution together with isobars and the Mach number distribution inside the whole nozzle. In the region adjacent to the inlet of the flat nozzle throat, the pressure variation in the radial direction is very large. The discontinuous nozzle area variation at Points B and C acts as an expansion corner [21] where isobars are bunched. Through the expansion wave zone at Point B the flow direction is gradually turned to align with the surface of the flat nozzle throat region and at Point C to the surface of divergent nozzle section. The presence of a hollow electrode in the supersonic region of the nozzle (the downstream electrode) generates a shock in front of it as shown in Figure 2, which propagates towards the nozzle wall and the nozzle axis. The presence of the upstream solid electrode causes flow to separate, thus creating a wake of almost constant pressure within which the flow circulates [22].
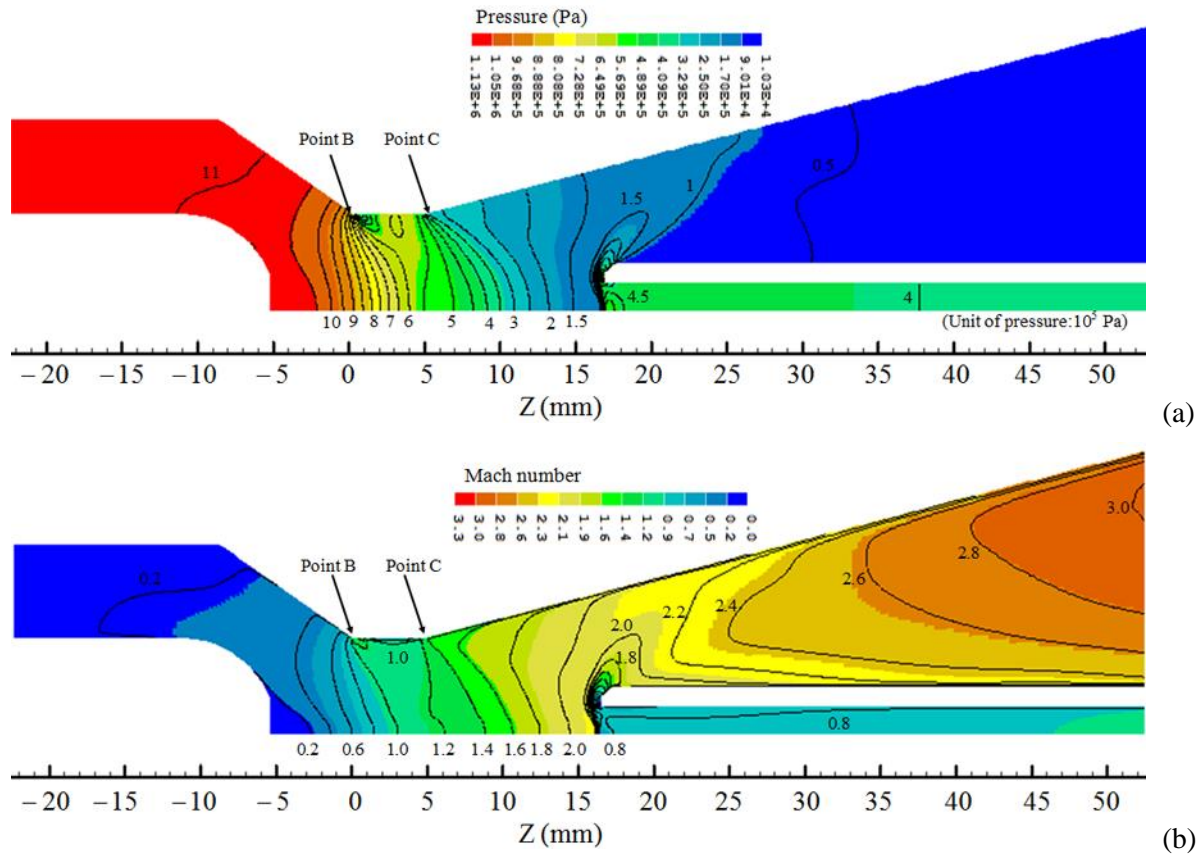
Figure 2. Pressure and Mach number distributions for the cold flow at P_0=11.2 atm. (a) Pressure distribution together with isobars and (b) Mach number distribution together with isobars.

4.1.2 Effects of the downstream electrode

The pressure distribution and the isobars near the downstream electrode are shown in Figure 3(a) and the Mach number together with the streamlines in Figure 3(b). The isobars in front of the flat surface 2-3 (Figure 3(a)) of the downstream electrode are very dense showing the existence of the shock. The variations of pressure and Mach number along the horizontal line passing the centre of Surface 2-3 (Line AA' in Figures 1 and 3) exhibit the features of a normal shock (Figure 4) [21]. A bow shock can therefore be identified in front of the hollow electrode tip, the compression region of which extends to the nozzle axis (Figure 3). The flow behind the bow shock but adjacent to Line AA' is similar to that near a stagnation point. Pressure decreases in the radial direction from the centre of Surface 2-3, thus ensuring the turning of the flow from that parallel to the axis to that nearly vertical along Surface 2-3. Pressure between the bow shock and Surface 3-4-5 increases in the direction normal to the bow shock but decreases along the bow shock surface to ensure the direction of the flow as required by the nozzle wall and Surface 4-5 (Figure 3b).
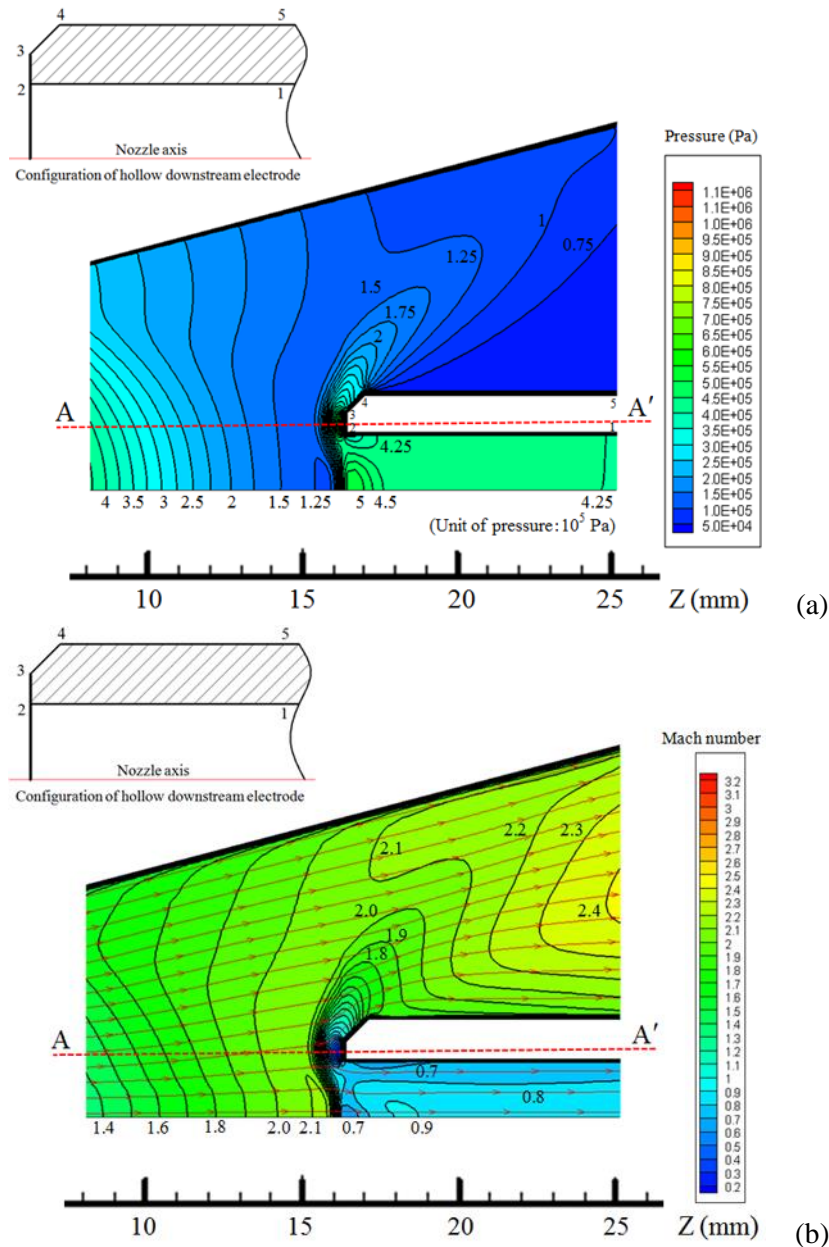
Figure 3. Flow pattern near the downstream electrode computed at P_0=11.2 atm. (a) Pressure distribution together with isobars and (b) Mach number distribution with constant Mach contours and flow streamlines.

Pressure along Line AA' (Figure 4a) and on the axis (Figure 4b) before the shock are almost identical for all flow models. However, the detailed shock structure in front of the downstream electrode tip (such as the isobar distribution shown in Figure 3a) and the flow behind the shock within the hollow region of the downstream electrode are dependent on the flow model. The results for laminar flow and those computed by the Chen-Kim model and RNG model are almost the same. This indicates that the effects of turbulence on the cold flow are negligible in the region not affected by the shock. The shock structure and the flow immediately behind the shock are known to be dependent on the turbulence models [23]. As no experimental results are reported in [1] for the cold nozzle flow, no conclusions regarding the accuracy of the flow models employed can be drawn. However, since the results of all turbulent models in the region away from the shock are almost identical with those of laminar flow the

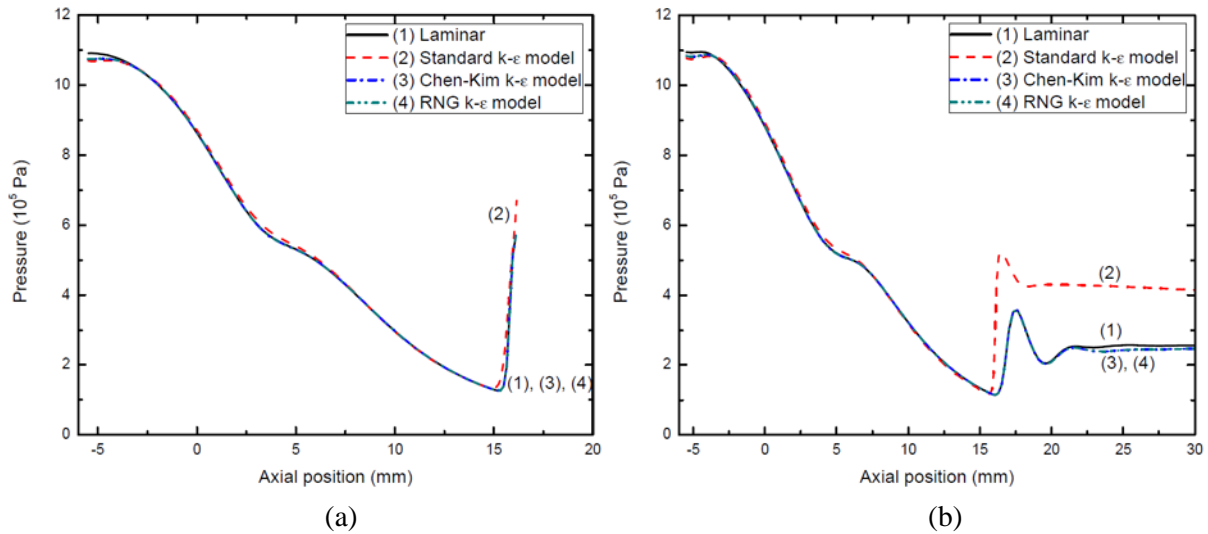shock structure predicted by the laminar flow model is perhaps closer to the reality.

(a)   (b)

Figure 4. Variations of pressure along Line AA' and the nozzle axis for the cold flow computed by different flow models at P_0=11.2 atm. (a) Pressure along Line AA' and (b) pressure along the nozzle axis.

4.1.3 Effects of the upstream electrode

Figure 5 shows the pressure distribution and streamlines near the upstream electrode and those in the transonic region of the nozzle. Close to Point D on the electrode surface the flow starts to separate, thus creating a wake region of approximately constant pressure (Figure 6) [22]. The flow circulates in the wake region. The flow separation point and the velocity and pressure inside the wake are known to be dependent on the flow model. However, the pressure differences in the wake predicted by different models are less than 2% of the absolute pressure within the wake. No experimental results are available at present to judge the relative merits of the flow models used. For the reason mentioned above results of the laminar flow model are expected to be closer to reality.
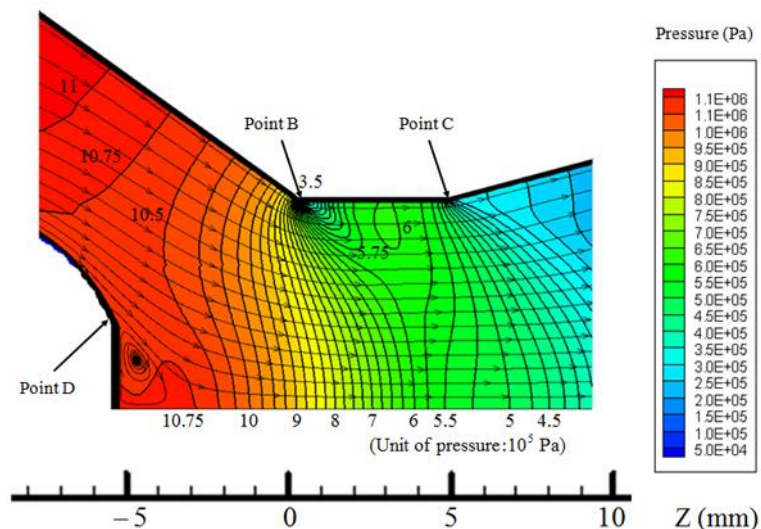

Figure 5. Pressure isobars and streamlines near the upstream electrode computed by the standard k-epsilon model at P_0=11.2 atm.
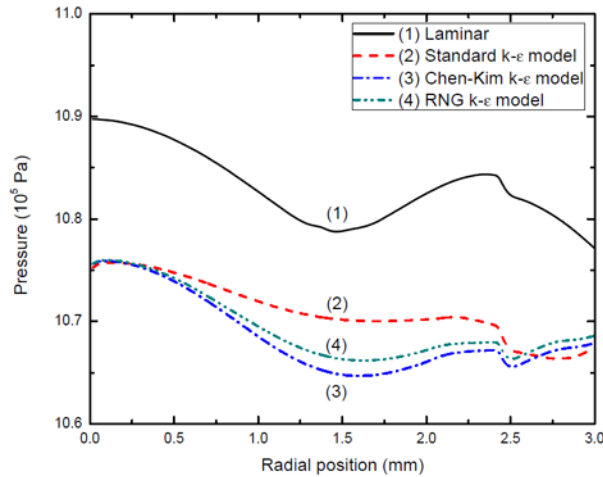
Figure 6. Radial distribution of pressure near the upstream electrode surface (Z= -5.0 mm) computed by different flow models at P_0=11.2 atm. Radial variation of pressure is less than 1% of the absolute pressure.

The wake near the upstream electrode and the shock region close to the downstream electrode are not expected to influence the thermal interruption capability of the nozzle interrupter (Figure 1) as the voltage drop in these two regions is expected to be much smaller than that of the arc column. However, these two regions can affect the dielectric strength of a breaker, the details of which will be given in Section 4.1.6.

4.1.5 The influence of stagnation pressure

For SF_6 the equation of state for ideal gas is valid for temperature up to 1000 K. The density of SF_6 is therefore proportional to pressure for a given temperature. Cold flow results indicate that the flow is mainly driven by pressure gradient and viscous stresses are negligible in comparison with pressure gradient. For turbulent flow Reynolds stress is proportional to density. Under these conditions it can easily be shown that the solutions of the conservation equations for laminar or turbulent flow are uniquely determined by normalized pressure P/P_0. Thus, velocity and Mach number are independent of stagnation pressure and the computed pressure expressed in normalized pressure is the same for any stagnation pressure. Computation results for stagnation pressures of 11.2 atm and 21.4 atm given in Figure 7 are in agreement with the above conclusions.
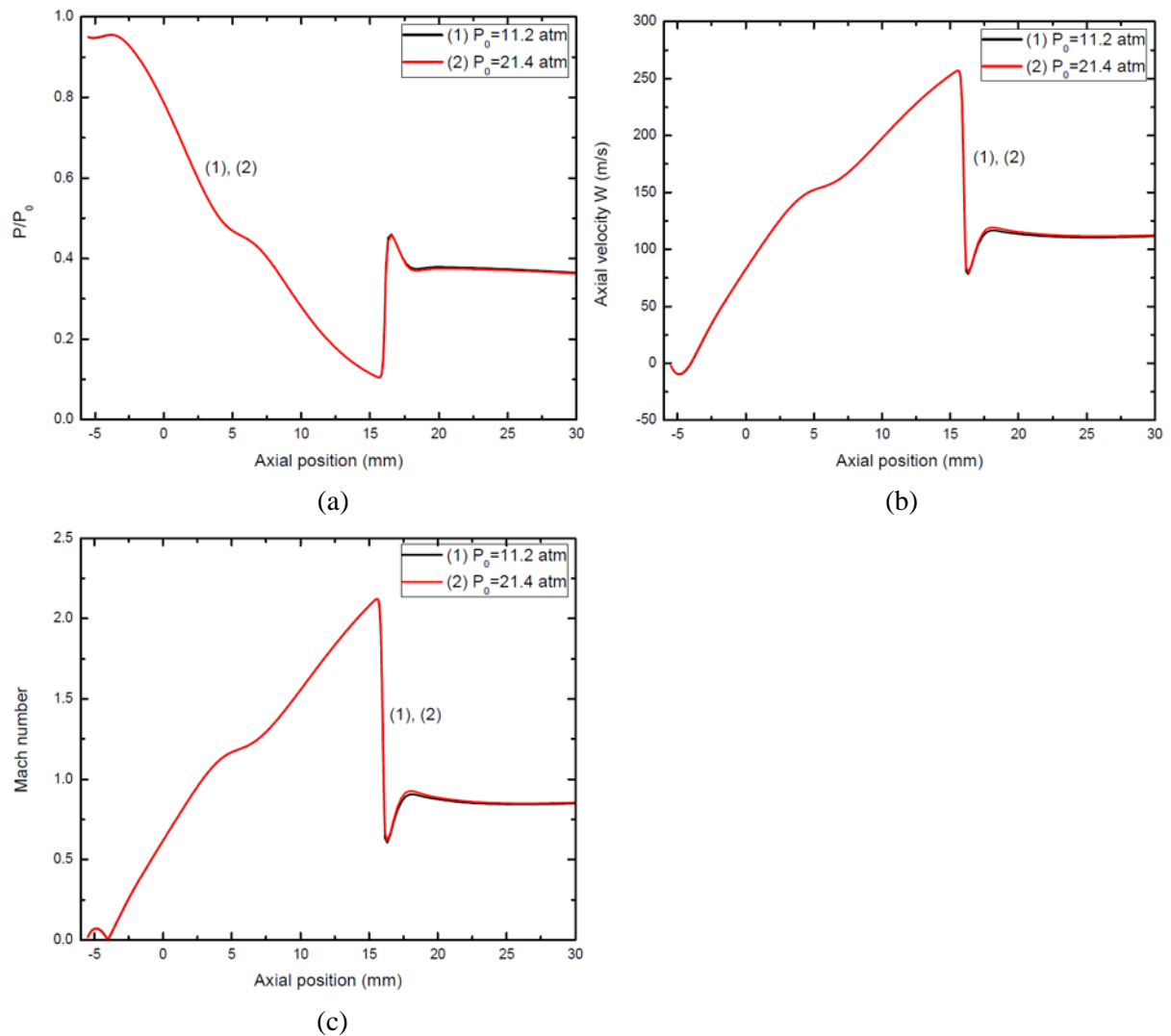
Figure 7. Comparison of (a) normalized pressure, (b) axial velocity and (c) Mach number along the nozzle axis for the cold flow at two stagnation pressures (P_0=11.2 and 21.4 atm). Standard k-epsilon model is used to obtain these results.

4.1.6 Electrode effects on dielectric strength

The dielectric strength of a nozzle interrupter immediately after the thermal extinction of the arc depends on the distribution of E/P between the two electrodes. The presence of the bow shock makes E/P highly non-uniform near the downstream electrode. The gas temperature of the circulating flow in the wake region near the upstream electrode immediately after arc interruption can be around 2000 K to 3000 K [24]. In such a hot gas there are still a large number of residue charge particles. The dielectric strength is therefore greatly reduced. It is important therefore to optimize the electrode configuration from cold flow point of view to ensure a smaller flow circulation region.

4.2 Characteristics of DC nozzle arcs

4.2.1 General features

Ohmic heating inside the arc creates a high temperature and low gas density region within the nozzle. The presence of the arc reduces the effective area for the flow, thus modifying the pressure distribution

within the nozzle, which in turn affects the arc [25]. The interaction between the arc and its surrounding cold flow determines the arc characteristics.

Present investigation covers a current range from 50 A to 1 kA. At 1 kA DC the arc cross section defined as the boundary of the 4000 K isotherm (hereafter referred to as the electrical boundary) at the stagnation pressure of 11.2 atm does not exceed 8% of the nozzle area (Figure 8). The disturbance to the cold flow due to the presence of the arc is quite small, which results in the pressure distribution within the nozzle to be nearly the same as that of cold flow except in the regions close to the two electrodes. The qualitative features of the nozzle arc predicted by various flow models are similar. Unless otherwise specified, the results given in this section are those obtained by the standard k-epsilon model.
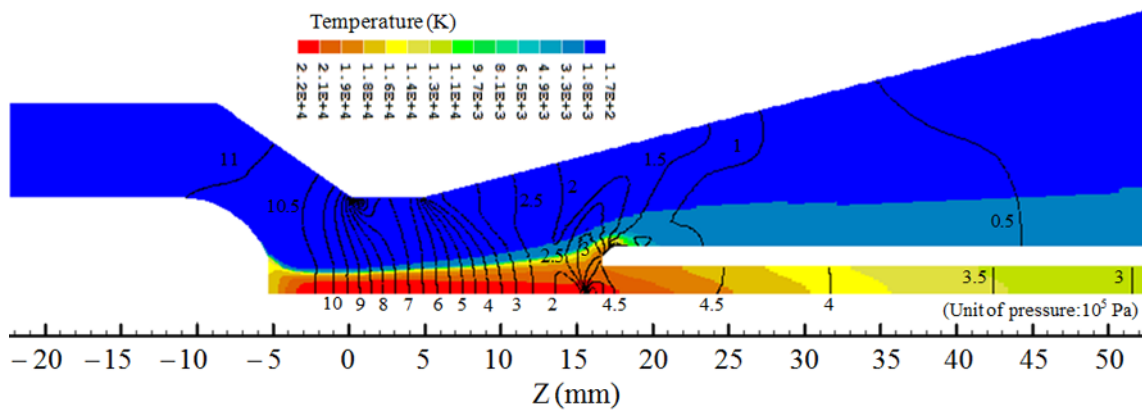

Figure 8. Temperature contour together with pressure isobars in the nozzle at 1 kA DC and at P_0=11.2 atm.
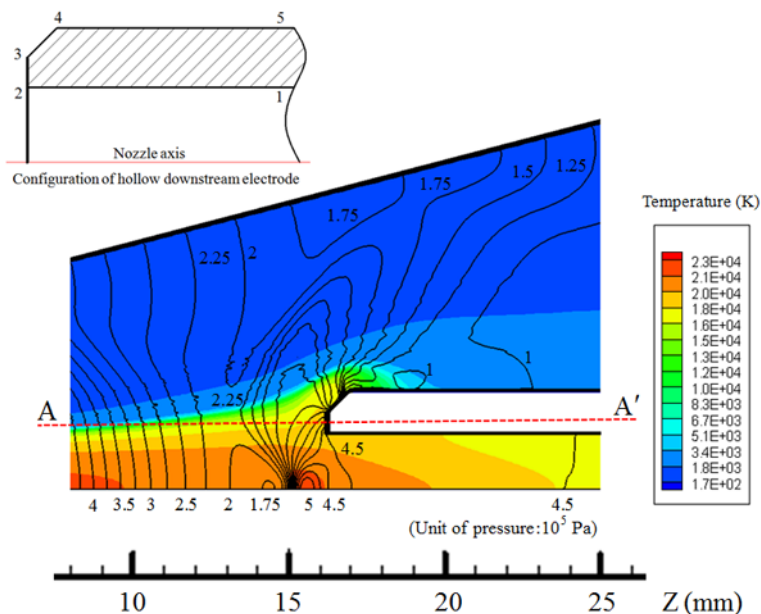

Figure 9. Temperature contour together with pressure isobars near the upstream electrode showing the formation of a compression region close to the tip of the downstream electrode.

The 1 kA DC arc greatly disturbs the flow near the downstream electrode tip. The hot plasma covers the downstream electrode tip, which renders the local flow subsonic. Since the flow needs to be

decelerated towards the surface of electrode in order to satisfy non-slip boundary condition for velocity, this creates a compression zone (Figures 9 and 10a) in front of the electrode tip. The pressure waves emanating from Surface 2-3-4 are bunched on the arc axis, thus creating a pressure distribution similar to a shock (Figures 9 and 10b). The bunching of the pressure waves is a direct consequence of the wave travelling towards the axis encountering a rising temperature, thus a region of increasing sound speed. The qualitative features of the shapes of the pressure isobars near the axis but originated from Surface 2-3-4 agree with the Snell's law of sound wave refraction [26].
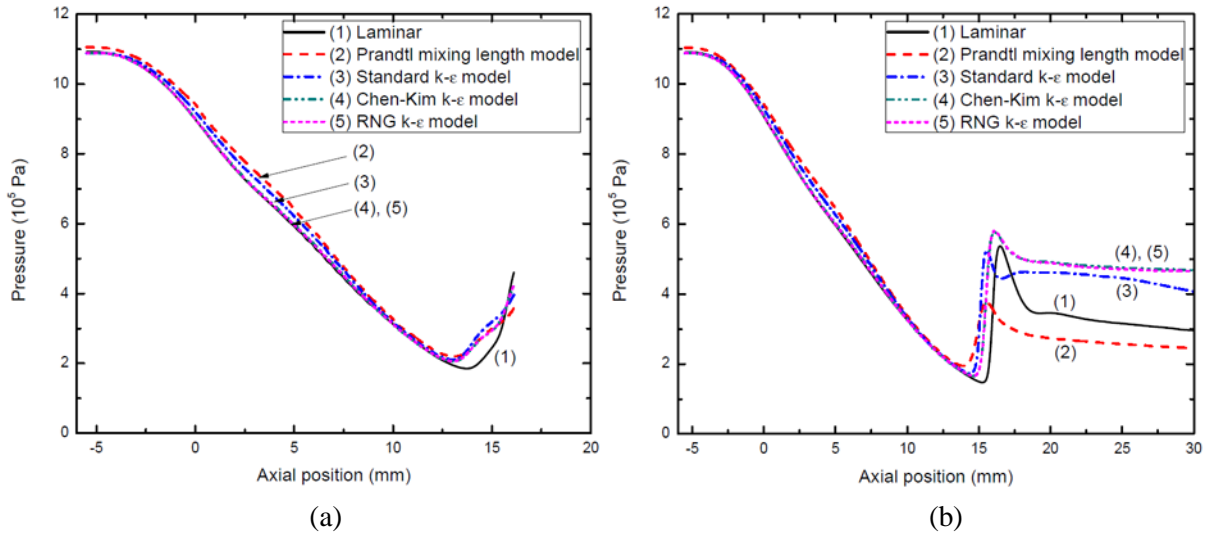

| (a) | (b) |

Figure 10. Variations of pressure along Line AA' and the nozzle axis computed by various flow models at 1kA DC and at P_0=11.2 atm. (a) Pressure along Line AA' and (b) pressure along the nozzle axis.

When current is decreased, the thermal influence region of the arc is reduced. At a current below 100 A the bow shock as observed in the cold flow reappears. This will be the likely case when the current is reduced to zero during the interruption of a fault current by a circuit breaker. The presence of the arc also affects the wake region near the upstream electrode tip. At 1 kA DC the wake no longer exists due to the presence of the arc. When the current is reduced the wake and flow circulating regions reappear as shown in Figure 11. Caution should be exercised regarding the accuracy of the prediction by various flow models used in present investigation. As previously indicated the flow in the regions close to electrodes is dependent on the flow models. In the absence of experimental results for the verification of flow models our discussion can only be regarded as qualitative in nature. However, the influence of the two electrode regions on the arc and the flow in the rest of the nozzle is small. They hardly affect the arc voltage as the voltage taken up by these two regions is negligible in comparison with the total arc voltage.
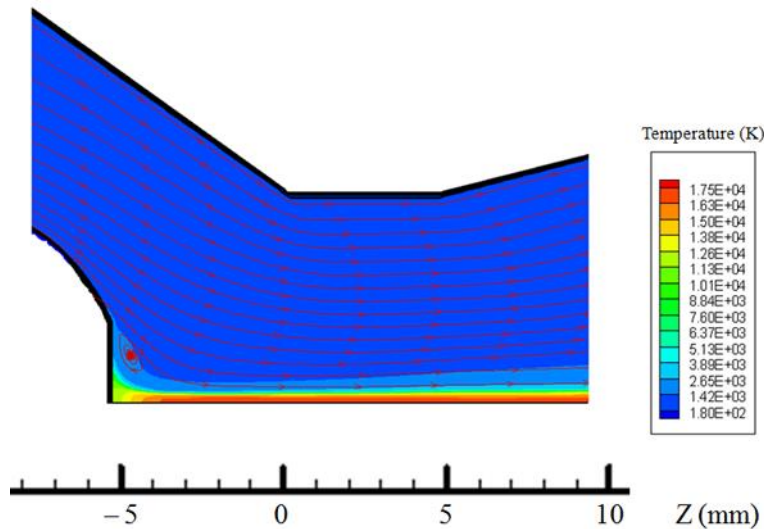
Figure 11. Temperature distribution together with the streamlines near the upstream electrode at 50 A DC and at P_0=11.2 atm.

4.2.2 DC arc voltage-current characteristics

The DC voltage-current (VI) characteristics of the nozzle arc computed by various flow models (Figure 12) are typical of high pressure arcs. When the current is large (600 A and above) the arc voltage is almost independent of current (the flat part of VI characteristics). For small currents it exhibits negative VI characteristics. The spread in arc voltages of the flat part of the VI characteristics predicted by all five flow models differ by less than 15% of the mean voltage. The mean voltage at a given current is the average of the voltages computed by the five flow models. This implies that turbulence does not play a dominant role in the determination of arc voltage. At low currents, arc voltage strongly depends on the flow models and the aforementioned spread increases to 35% of the mean at 50 A (Figure 12). The physical processes responsible for these features of the VI characteristics and the voltage spread by various flow models are discussed in the following two subsections.
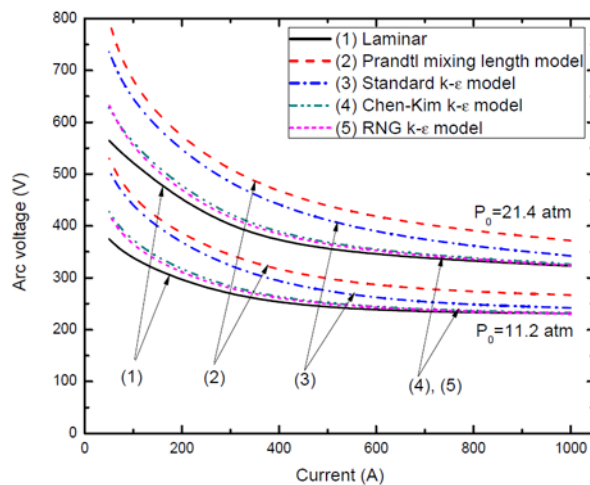

Figure 12. The voltage-current (VI) characteristics for the DC arcs computed by 5 flow models at two stagnation pressures.

4.2.3 Characteristics of nozzle arc with radiation dominated high temperature core

Examination of the computational results for the flat part of the VI characteristics given by various flow models shows that the axis temperature for currents 600 A and above is not sensitive to current. Typical axial variation of axis temperature for this current range is shown in Figure 13a although the results are for 1 kA. Excluding the regions close to the two electrodes axis temperature difference calculated by the different flow models is less than 5% of the mean temperature. Arc radius as defined by the radial position of the 4000 K isotherm is found to be proportional to the square root of the current (Figure 13b) for a given stagnation pressure.
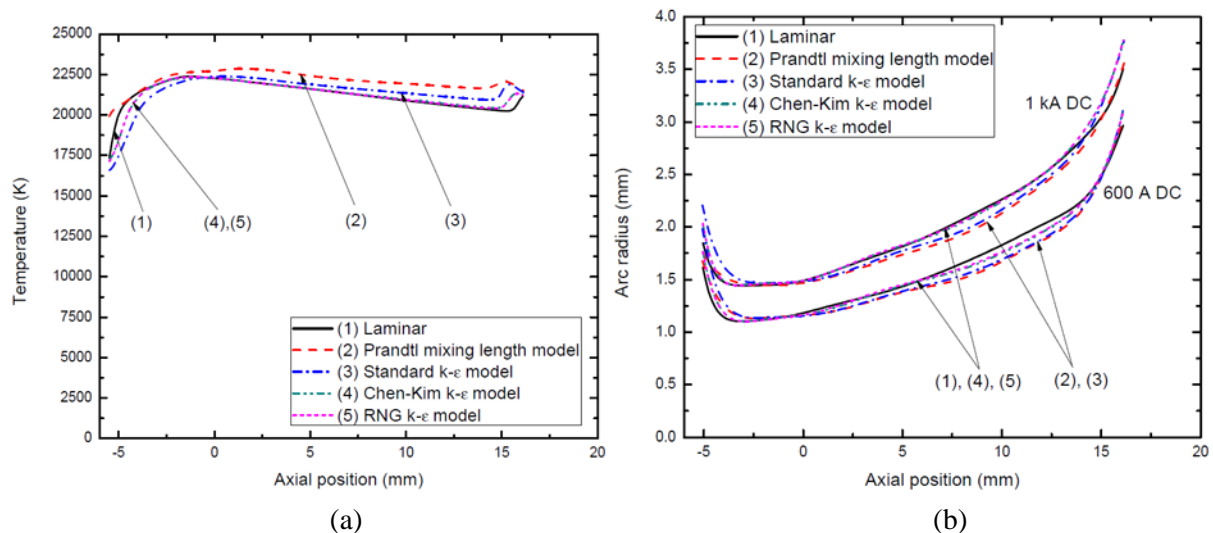

Figure 13. Variations of axis temperature and arc radius for currents 600 A and above at P_0=11.2 atm. (a) Axis temperature at 1 k A DC and (b) arc radius at 1 kA DC and 600 A DC.

Electrical field at an axial position not only depends on the axis temperature and arc radius but also on the radial temperature profile. Typical radial temperature profiles are given in Figure 14 which shows the temperature profiles at 1 kA DC for two typical axial positions corresponding to the nozzle throat region (Z=2.3 mm) and the region downstream of the nozzle throat (Z=7.9 mm). The temperature profile inside the arc core is rather flat. The boundary of arc core is defined as the radial position corresponding to a temperature of 83.3% of the axis temperature [15] (henceforth known as the core boundary). Such flat temperature profile indicates that within the core radiation transport is dominant. On the axis Ohmic input is balanced by net radiation loss, which determines the axis temperature for known Ohmic input. The energy balance at the core boundary for the whole arc is given in Table 2 for all flow models used.
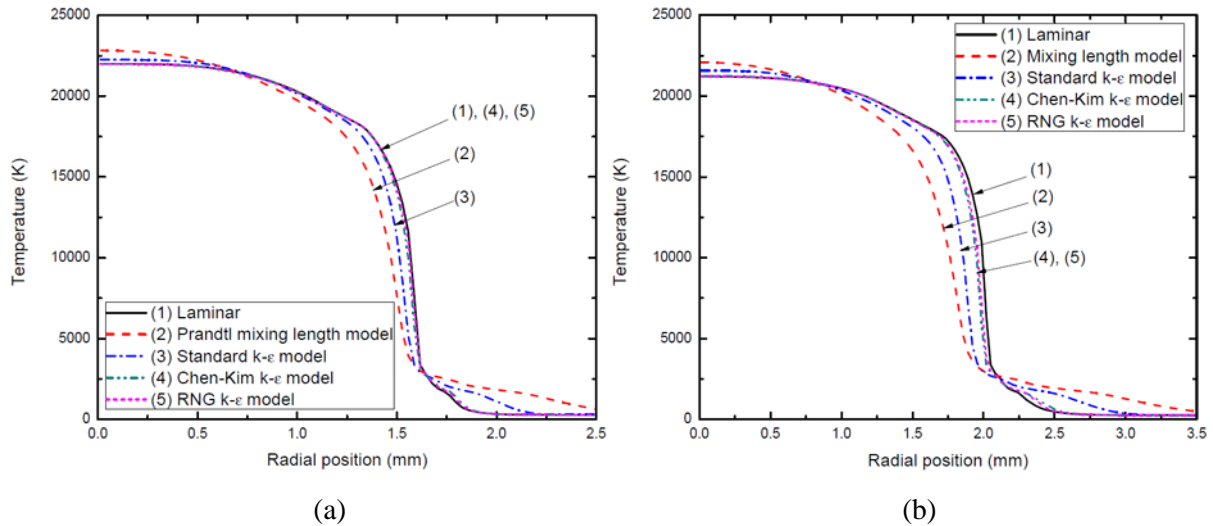
Figure 14. Radial temperature profiles at two axial positions computed by 5 flow models at 1 kA DC and at P_0=11.2 atm. (a) Z=2.3 mm and (b) Z= 7.9mm.

Table 2 shows that for all flow models the dominant energy loss process is due to radiation. For the Prandtl mixing length model and the standard k-epsilon model radial thermal conduction (nearly all due to turbulent heat conduction) accounts respectively for 24.3% and 13.8% of Ohmic input. Thus, the radial temperature gradients of the profiles predicted by these two models are greater than those predicted by other flow models as shown in Figure 14. The results of Chen-Kim model and those of RNG model are almost identical which are in turn very close to the results given by the laminar flow model. Although there is a large difference between the relative importances of various energy loss processes predicted by the five flow models (Table 2), the differences in electrical power input predicted by different flow models are very small. This is due to the very small differences in axis temperatures and in the core sizes (Figure 14) computed by various flow models. This results in nearly equal arc conductance. Since 80% of the current is carried by this core, the arc voltages predicted by various flow models are therefore very close to each other.

Table 2. Percentage of electrical power input associated with various energy transport processes for the whole arc length at the core boundary calculated by various flow models at 1 kA DC and P_0=11.2 atm. The power associated with the pressure work is not shown as it only accounts for 5 to 7% of the power input. This applies to all tables. Positive means power input and negative power loss.

Model	Power input (10^5 W)	Radial thermal conduction	Radiation loss	Axial enthalpy convection	Radial enthalpy convection
(1)	1.89	-4.1%	-67.7%	-19.1%	-1.7%
(2)	1.88	-24.3%	-62.8%	-4.5%	-4.3%
(3)	1.90	-13.8%	-66.8%	-10.9%	-4.0%
(4)	1.87	-4.8%	-70.1%	-15.3%	-4.8%
(5)	1.87	-4.6%	-70.1%	-15.1%	-5.0%

Method of calculation: Power input $= \int_{Z1}^{Z2}\left[\int_{0}^{R}\sigma E^2 2\pi r dr\right]dz$,

$$\text{Radiation loss}=-\int_{Z1}^{Z2}\left[\int_{0}^{R} q2\pi r dr\right]dz\Big/\text{Power input}\,,$$

$$\text{Radial thermal conduction}=\int_{Z1}^{Z2}\left[\int_{0}^{R}\frac{1}{r}\frac{\partial}{\partial r}\left(r\frac{k}{c_p}\frac{\partial h}{\partial r}\right)2\pi r dr\right]dz\Big/\text{Power input}$$

$$\text{Axial enthalpy convection}=-\int_{Z1}^{Z2}\left[\int_{0}^{R}\rho w\frac{\partial h}{\partial z}2\pi r dr\right]dz\Big/\text{Power input}$$

$$\text{Radial enthalpy convection}=-\int_{Z1}^{Z2}\left[\int_{0}^{R}\rho v\frac{\partial h}{\partial r}2\pi r dr\right]dz\Big/\text{Power input}$$

where R refers to the radial position of the core boundary or electrical boundary (Table 3) and (Z2-Z1) the arc length.

Key to the models: (1) Laminar flow model, (2) Prandtl mixing length model, (3) Standard k-epsilon model, (4) Chen-Kim k-epsilon model and (5) RNG k-epsilon model.

To assess the influence of turbulence we need to know the arc energy balance at the electrical boundary. This is because between the arc core boundary and the electrical boundary nearly 80% of the radiation flux coming out of the arc core is absorbed in this region, thus altering the energy balance. Table 3 shows how electrical power input into the electrically conducting core is balanced by various energy transport processes.

Table 3. Percentage of electrical power input associated with various energy transport processes for the whole arc length at the electrical boundary calculated by 5 flow models at 1 kA DC and P_0=11.2 atm. Mathematical expressions for power input and power loss and the key to the models are the same as those in Table 2.

Model	Power input (10^5 W)	Radial thermal conduction	Radiation loss	Axial enthalpy conduction	Radial enthalpy convection
(1)	2.29	-1.2%	-25.1%	-91.9%	24.7%
(2)	2.65	-50.6%	-12.2%	-48.7%	17.9%
(3)	2.41	-30.6%	-18.3%	-66.4%	23.2%
(4)	2.30	-8.8%	-23.5%	-82.6%	22.8%
(5)	2.29	-8.2%	-23.6%	-83.1%	22.4%

Due to the radiation absorption the energy balance at the electrical boundary has been greatly altered in comparison with that at the core boundary. For laminar flow, Chen-Kim and RNG models, electrical power input is balanced by radiation and axial and radial convections while thermal conduction has the least influence on energy balance. For the Prandtl mixing length model and the standard k-epsilon model radial thermal conduction and axial convection are the most important energy loss processes although the turbulence effect as predicted by the Prandtl mixing length model is much stronger than that of the standard k-epsilon model.

The modifications to the dissipation rate equation of the standard k-epsilon model by Chen-Kim and RNG models are intended to increase the dissipation rate, thus reducing the turbulence. The complex non-linear interactions between average turbulent kinetic energy, the mean flow, and the dissipation rate result in a much reduced average kinetic energy (Figure 15) and dissipation rate (Figure 16) for Chen-Kim and RNG models as compared with those of the standard k-epsilon model. It should be noted that turbulence intensity increases towards the downstream electrode due to the axial development of turbulence (Figure 15b).
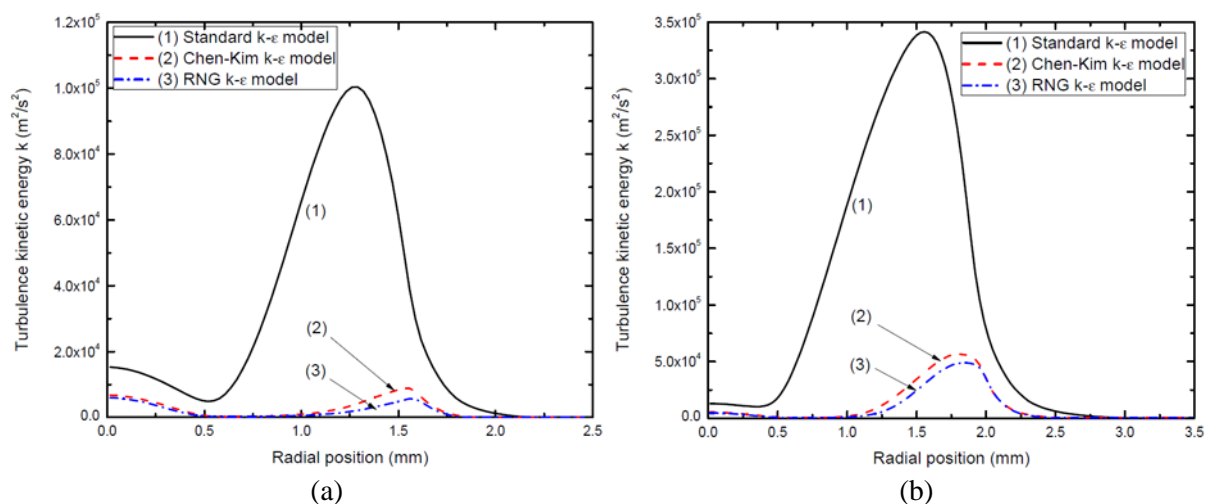

(a)   (b)

Figure 15. Radial profiles of turbulence kinetic energy at two axial positions computed by three flow models at 1 kA DC and at P_0=11.2 atm. (a) Z=2.3 mm and (b) Z= 7.9mm.
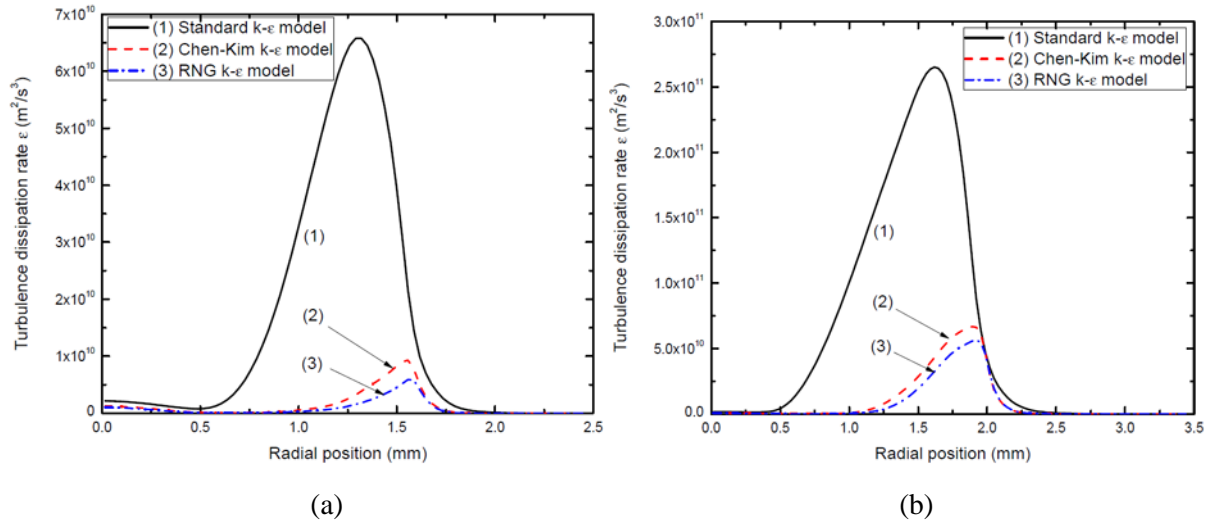
(a)   (b)

Figure 16. Radial profiles of turbulence dissipation rate at two axial positions computed by three flow models at 1 kA DC and at P_0=11.2 atm. (a) Z=2.3 mm and (b) Z= 7.9mm.

The radial distributions of the average turbulent kinetic energy and the dissipation rate have two peaks, one of which is on the nozzle axis and the other in the region where velocity reduces rapidly (Figure 17). Careful examination of the results show that the first peak on the nozzle axis is attributed to the axial gradient of axial velocity (dw/dz) and the other peak is due to the large radial gradient of axial velocity (Figure 17). Both velocity gradients affect the distributions of the average turbulent kinetic energy and the dissipation rate through the rate of generation of turbulent kinetic energy given by equation (11).
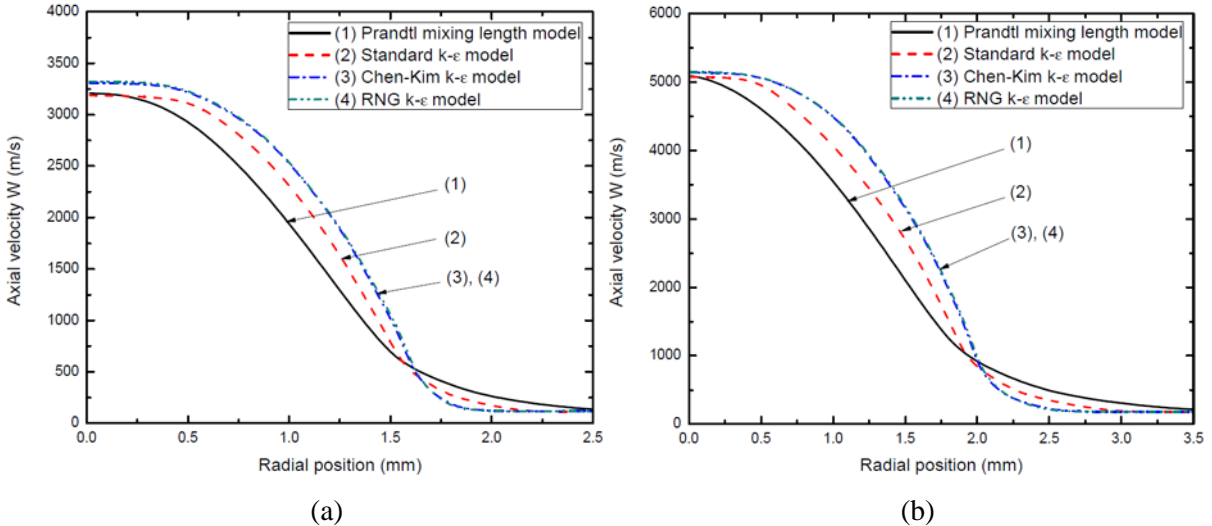

(a)   (b)

Figure 17. Radial profiles of axial velocity at two axial positions computed by 4 flow models at 1 kA DC and at P_0=11.2 atm. (a) Mid nozzle throat (Z=2.3 mm) and (b) Z= 7.9mm.

Turbulence enhanced momentum and energy transports are determined respectively by eddy viscosity μ_t and k_t/c_p in momentum and energy conservation equations. Since k_t/c_p is directly related to μ_t through turbulent Prandtl number it is suffice to examine μ_t (Figure 18) in order to see why the four turbulences models give widely different turbulence levels. Chen-Kim and RNG models give the

smallest values of μ_t, hence the lowest level of turbulence. The Prandtl mixing length model has the largest μ_t because of the adoption of the thermal radius of the arc as the turbulence length scale, which is larger than the length scales computed by the other three turbulence models (Figure 19). μ_t inside the arc core computed by 4 turbulence models are all very low. This means that the large eddies generated in the region where radial velocity gradient is high cannot easily penetrate the arc core region, thus rendering radiation transport being dominant.

Arcs in the current range corresponding to the flat part of VI characteristics exhibit similar features to those of the 1 kA DC arc. For the flat part of the V-I characteristic, Ohmic input on the axis is entirely balanced by radiation. When current is reduced, the required adjustment in axis temperature in order for the net radiation loss to balance the reduced Ohmic input is very small. This is because for a small change in temperature net radiation loss of SF_6 changes by a large amount for temperatures above 20000 K [27]. This explains why the axis temperature of a 600 A arc is almost the same as that of 1 kA. Since the arc cross section is proportional to the current and the arc temperature within the core is not sensitive to the current, arc voltage is therefore almost independent of the current.
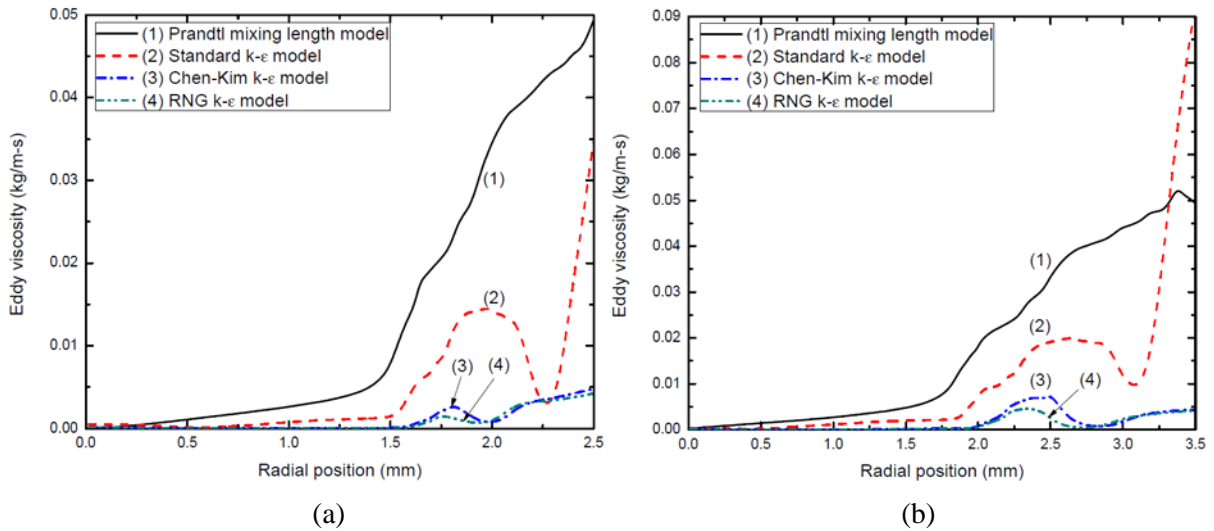

Figure 18. Radial profiles of the eddy viscosity (μ_t) at two axial positions computed by 4 flow models at 1 kA DC and at P_0=11.2 atm. (a) Z=2.3 mm and (b) Z= 7.9mm.
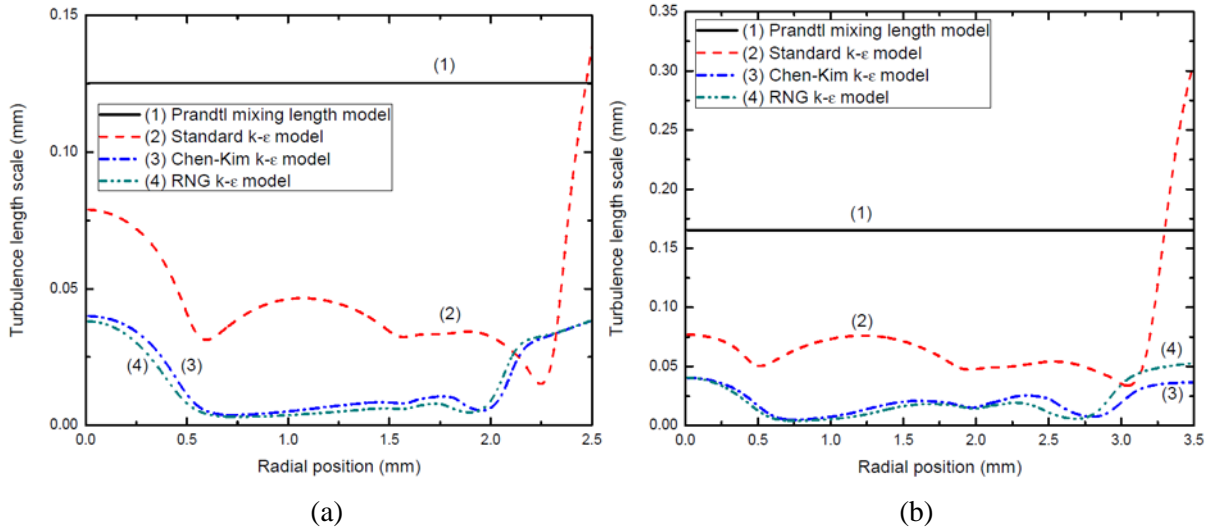
(a)   (b)

Figure 19. Radial profiles of turbulence length scale at two axial positions computed by 4 flow models at 1 kA DC and at P_0=11.2 atm. (a) Z=2.3 mm and (b) Z= 7.9mm.

4.2.4 Characteristics of nozzle arc with radiation and thermal conduction dominated high temperature core

The arc voltage increases with decreasing current for currents below 600 A. The axis temperature at 300 A is reduced to 17000 K (Figure 20) due to reduced Ohmic input. When the arc size is reduced, radial thermal conduction in the high temperature core is expected to become more important for two reasons: firstly, the relative importance of thermal conduction (energy taken out from a surface) to radiation loss (energy loss related to the volumetric effect) is inversely proportional to the arc radius, and, secondly, net radiation loss decreases rapidly with temperature for temperature below 18000 K [27]. In the core region thermal conduction is appreciable (Table 4). The radial temperature profile in the high temperature core is no longer flat especially near the core boundary (Figure 21). There is considerable radial temperature gradient inside the arc core (Figure 21). It has also been found that the dependence of arc cross section with current is stronger than the linear relationship found for the flat part of the VI characteristics. Thus, the rate of reduction in arc conductance due to decreases in arc temperature and in arc radius is faster than the rate of current reduction. Therefore arc voltage increases with decreasing current giving rise to negative VI characteristics.
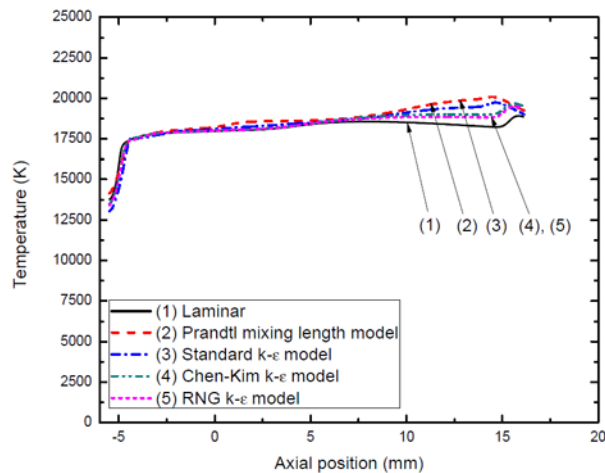

Figure 20. Variations of axis temperature at 300 A DC and P_0=11.2 atm.

Table 4. Percentage of electrical power input associated with various energy transport processes for the whole arc length at the core boundary calculated by various flow models at 50 A DC and P_0=11.2 atm. Mathematical expressions for power input and power loss and the key to the models are the same as those in Table 2.

Model	Power input (10^4 W)	Radial thermal conduction	Radiation loss	Axial enthalpy conduction	Radial enthalpy convection
(1)	1.72	-24.9%	-66.7%	-3.5%	-0.82%
(2)	2.08	-54.9%	-46.0%	2.5%	1.1%
(3)	2.13	-47.1%	-51.4%	-0.7%	1.3%
(4)	1.91	-34.0%	-61.8%	-1.2%	0.05%
(5)	1.89	-34.7%	-61.3%	-1.0%	0.15%

Detailed energy balance calculations at the high temperature core boundary by various flow models (Table 4) at 50 A DC confirm the dominance of thermal conduction and radiation. For laminar flow model and turbulent flow models other than the Prandtl mixing length model, radiation at the core boundary is still the most important energy loss mechanism. Energy balance at the electrical boundary (Table 5) reveals that for the Prandtl mixing length model and the standard k-epsilion model turbulent thermal conduction is the dominate energy loss process while for laminar flow and the Chen-Kim and RNG models radiation loss is the most important. The reason for such a difference in dominant energy loss mechanisms between different flow models is the intensity of turbulence. Turbulence intensity is determined by the eddy viscosity. Radial profiles of eddy viscosity at two axial positions are given in Figure 22 with μ_t predicted by the Prandtl mixing length model the largest. It should also be noted that at the electrical boundary axial convection is nearly balanced by radial convection (Table 5).
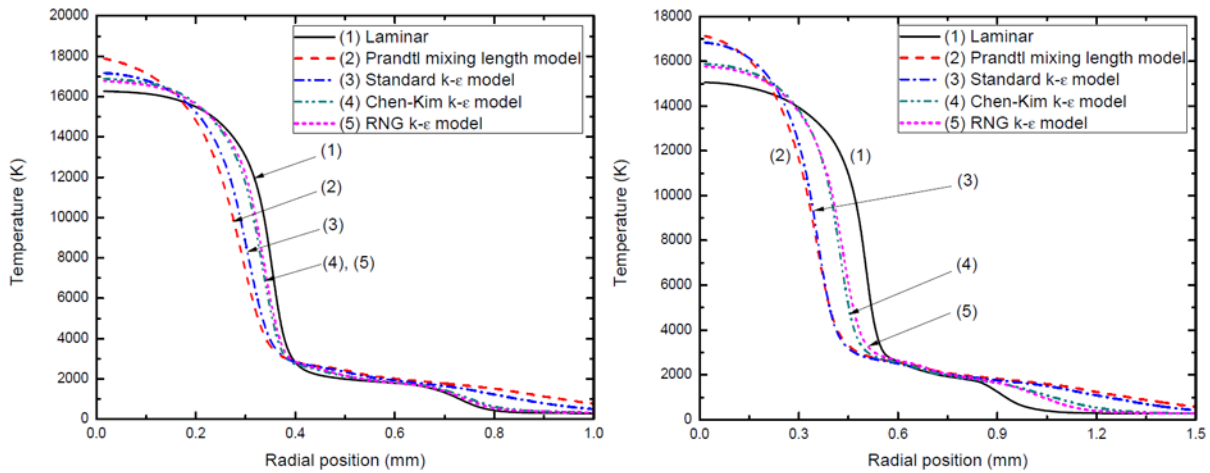

Figure 21. Radial temperature profiles computed by the four turbulence models at two axial positions at 50 A DC. P_0=11.2 atm. (a) Z=2.3 mm and (b) Z=7.9mm.

Table 5. Percentage of electrical power input associated with various energy transport processes for the whole arc length at the electrical boundary calculated by various flow models at 50 A DC and P_0=11.2 atm. Mathematical expressions for power input and power loss and the key to the models are the same as those in Table 2.

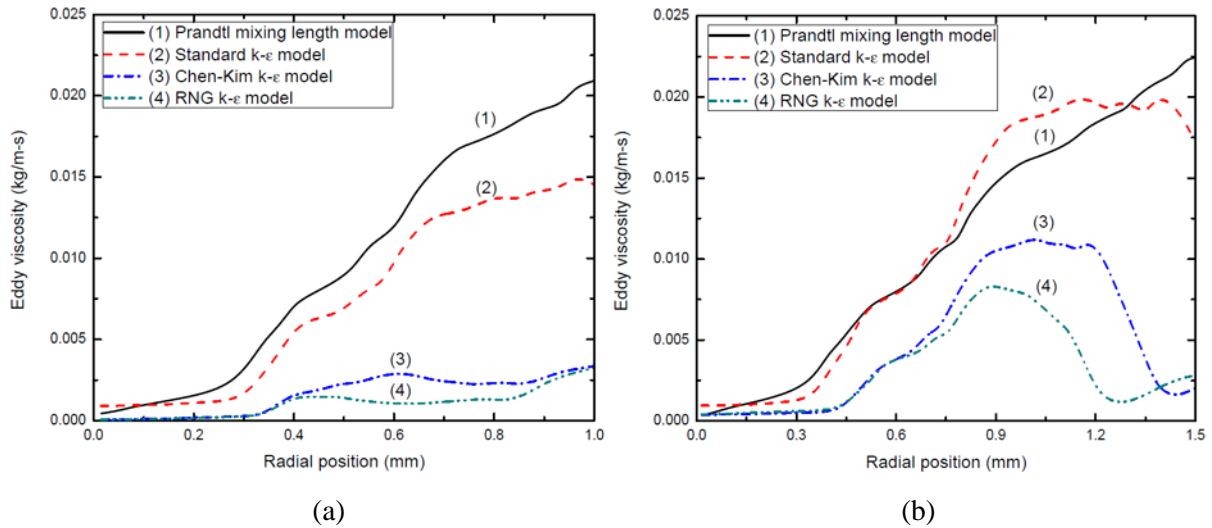| Model	Power input (10^5 W)	Radial thermal conduction	Radiation loss	Axial enthalpy conduction	Radial enthalpy convection
(1)	1.87	-4.3%	-56.6%	-67.7%	32.7%
(2)	2.62	-62.6%	-31.1%	-17.2%	13.6%
(3)	2.51	-55.8%	-38.7%	-15.9%	14.2%
(4)	2.13	-33.8%	-50.0%	-31.0%	18.8%
(5)	2.12	-35.5%	-48.9%	-30.0%	18.3%

(a)　　　　　　　　　　　　　　(b)

Figure 22. Radial profiles of the eddy viscosity at two axial positions computed by various flow models at 50 A DC and at P_0=11.2 atm. (a) Z=2.3 mm and (b) Z= 7.9mm.

4.2.5 The effects of the stagnation pressure P_0

For higher stagnation pressures (e.g. P_0=21.4 atm), the qualitative features of the arc and its surrounding flow are similar to those of 11.2 atm for all flow models used. Within the range of current investigated (50 A to 1 kA), the arc voltage is found to be approximately proportional to the square root of the stagnation pressure irrespective of the flow models (Figure 12). This is in agreement with the voltage- stagnation pressure scaling law derived from the arc integral analysis [25]. The axis temperature does not appear to be sensitive to the stagnation pressure for a given current, while the arc radius is found to be inversely proportional to $(P_0)^{0.25}$.

Relative importance of various energy transport processes at the core boundary and at the electrical boundary remain the same as those given in Tables 2 to 5 although the percentage of electrical power taken out by radiation loss is slightly increased due to increased radiation with pressure and reduction in arc size.

5 Conclusions

The cold flow and the arc under direct currents burning in the nozzle of [1] with fixed stagnation pressure have been investigated computationally using five flow models, which include laminar flow model, the Prandtl mixing length model, the standard k-epsilon model and its two variant, Chen-Kim model and the RNG model.

Four flow models, excluding the Prandtl mixing length model, are used to simulate the cold flow insider the nozzle. These models give nearly the same results except in the region close to the two electrodes. This indicates that under the experimental conditions of [1] turbulence is not important for the bulk of the cold flow. There is a bow shock in front of the downstream hollow electrode and a wake near the tip of the upstream electrode. However, the size of the wake and the strength and the structure of the shock differ widely between flow models. The implications of the wake and shock on dielectric breakdown have been discussed. The Prandtl mixing length model is not suitable for the computation of the cold internal flow inside a nozzle as the length scale for turbulence cannot be defined in the absence of the arc.

The VI characteristic of the nozzle arc consists of a flat part (current not less than 600A) where the arc voltage is independent of current and a part with negative VI characteristic where the arc voltage rises when current is reduced. On the flat part of the VI characteristic, radiation is the dominant energy transport process within the arc core, which results in a rather flat radial temperature profile inside the core. The axis temperature is almost independent of current and the arc cross section proportional to current, thus resulting in a constant arc voltage. Such features are only for discharge conditions under which Lorentz force can be neglected and arc radiation induced ablation is absent. The arc voltages predicted by various flow models differ within 15% of the mean voltage. Since Ohmic input into the core is taken out mainly by radiation transport and 80% of the current is conducted within the core, turbulence has little influence on arc voltage. Thus, arc voltage at high current is not an effective means for the verification of flow models. For currents above 600A the bow shock and the wake region near the electrodes disappear as the presence of the arc greatly modifies the flow close to the electrodes.

When current is reduced below 600A, thermal conduction and radiation inside the arc core are dominant energy transport mechanisms. The radial temperature profile becomes peaky and constricted as required by thermal conduction. The axis temperature decreases with current. The dependence of arc conductance on the current is stronger than the linear relationship found for the flat part of the VI characteristic, thus giving rise to negative VI characteristic. Arc voltage depends on the flow model and there is a large difference between the voltage predicted by the Prandtl mixing length model and that by laminar flow model.

The qualitative features of the arc at a given current but with different stagnation pressures are the same. Arc voltage has been found to be proportional to the square root of stagnation pressure.

A detailed examination has been conducted to find the causes why the turbulence intensities predicted by different turbulence models vary a great deal. As turbulence enhanced moment and heat transfes depend on eddy viscosity, the eddy viscosity predicted by the Prandtl mixing length model is the

largest since it uses the arc's thermal radius as its turbulence length scale. The Chen-Kim model and the RNG model give almost the same eddy viscosity which is much smaller than that predicted by the standard k-epsilon model due to the additional term added to the dissipation rate equation of the standard k-epsilon model. As there are no DC arc voltage measurements available to verify turbulence models the discussion on the relative merits of the flow models will be deferred to Part II of this series of papers where the predicted RRRV by various models will be compared with the test results of [1]. RRRV is determined by the arc behaviour during current zero period where current is small. The correct prediction of RRRV is a critical test for turbulence models as arc voltage at high currents are not sensitive to the flow models.

References

[1] Benenson D M, Frind G, Kinsinger R E, Nagamatsu H T, Noeske H O and Sheer, Jr R E 1980 Fundamental investigation of arc interruption in gas flows EPRI EL-1455 (Project 246-2)

[2] Fang M T C, Zhuang Q and Guo X J 1994 Current zero behaviour of an SF_6 gas-blast arc Part II: turbulent flow *J. Phys. D: Appl. Phys.* **27** 74-83

[3] Hermann W, Kogelschatz U, Niemyer L, Ragaller K and Schade E 1976 Investigation on the phenomena around current zero in HV gas blast circuit breakers *IEEE Trans. Power Appr. Syst.* **95** 1165-76

[4] Cowley M D 1974 Integral methods of analysing electric arcs: I. Formulation *J. Phys. D: Appl. Phys.* **7** 2218-22

[5] Yan J D, Nuttall K I and Fang M T C 1999 A comparative study of turbulence models for SF_6 arcs in a supersonic nozzle *J. Phys. D: Appl. Phys.* **32** 1401-6

[6] Song K D, Lee B Y and Park K Y 2004 Calculation of the post-arc current in a supersonic nozzle by using the K-epsilon model *Journal of Korean Physical Society.* **45** 1537-43

[7] Versteeg H K and Malalasekera W 2007 An introduction of computational fluid dynamics: the finite volume method (second edition), Pearson Education Limited

[8] Launder B E and D B Spalding 1974 The numerical computation of turbulent flows *Computer Methods in Applied Mechanics and Engineering.* **3** 269-89

[9] Yakhot V, Orszag S A, Thangam S, Gatski T B and Speziale C G 1992 Development of turbulence models for shear flows by a double expansion technique *Phys.Fluids A.* **4** 1510-20

[10] Chen Y S and Kim S W Computation of turbulent flows using an extended K-epsilon turbulence closure model, Interim report, NASA, CR-179204

[11] Zhou Q, Li H, Xu X, Liu F, Guo S, Chang X, Guo W and Xu P 2009 Comparative study of turbulence models on highly constricted plasma cutting arc *J. Phys. D: Appl. Phys.* **42** 1-14

[12] El-Hadj A A and Ait-Messaoudene 2005 Comparison between two models and analysis of the effect of the substrate movement on the flow field of a plasma jet *Plasma Chemist. and Plasma Process.* **25** 699-722

[13] Bini R, Basse N T and Seeger M, 2011 Arc induced turbulent mixing in an SF_6 circuit breaker model *J. Phys. D: Appl. Phys.* **44** 025203

[14] Zhang Q, Yan J D and Fang M T C 2012 Modelling of turbulent arc burning in a supersonic nozzle *Proc. Int.Conf. on Gas Discharges and Their Applications (Beijing) (High VoltageEngineeing: Special Issue on Gas Discharges and Their Applications* vol 38*)* pp 202-5

[15] Zhang J F, Fang M T C and Newland D B 1987 Theoretical investigation of a 2kA arc in a

supersonic nozzle *J. Phys. D: Appl. Phys.* **20** 368-79

[16] Frost L S and Liebermann R W 1971 Composition and transport properties of SF_6 and their use in a simplified enthalpy flow arc model *Proc. IEEE.* **59** 474-85

[17] Turbulence models in PHOENICS

[18] Zhang Q, Yan J D and Fang M T C 2013 Current zero behaviour of and SF6 nozzle arc under shock conditions *J. Phys. D: Appl. Phys.* **46** 165203

[19] Boundary conditions in PHOENICS. Retrieved from: http://www.cham.co.uk/phoenics/d_polis/d_lecs/general/bcond.htm

[20] Guidelines for Specification of Turbulence at Inflow Boundaries. Retrieved from: http://www.esi-cfd.com/esi-users/turb_parameters/

[21] Anderson J D 2003 Modern compressible flow (3rd Edition), McGraw-Hill

[22] Shayler P J and Fang M T C 1980 Flow near the upstream electrode of gas-blast circuit breakers *Proc. IEE.* **127** 26-32

[23] Balabel A, Hegab A M, Nasr M and Samy M El-Behery 2011 Assessment of turbulence modeling for gas flow in two-dimensional convergent-divergent rocket nozzle *Applied Mathematical Modelling.* **35** 3408-22

[24] Yan J D, Fang M T C and Liu Q S 1997 Dielectric breakdown of a residue SF_6 plasma at 3000 K under diatomic equilibrium *IEEE Trans. Dielectrics and Electrical Insulation.* **4** 114-9

[25] Fang M T C, Ramakrishnan S and Messerle H K 1980 Scaling laws for gas-blast circuit-breaker arcs during the high current phase *IEEE Trans. Plasma Sci.* **PS-8** 357-62

[26] Stephens R W B and Bate A E 1966 Acoustics and vibrational physics

[27] Liebermann R W and Lowke J J 1976 Radiation emission coefficients for sulfur hexafluoride arc plasmas *J. Quant. Spectrosc. Radiat. Transf.* **17** 253-64

[28] Yan J D, Fang M T C and Hall W 1999 The development of PC based CAD tools for auto-expansion circuit breaker design IEEE Transactions on Power Delivery, **14** 176-181